Optics Communications 591 (2025) 132185

Contents lists available at ScienceDirect

Optics Communications

journal homepage: www.elsevier.com/locate/optcom

Optimized wide-angle metamaterial bandpass filters with multi-layer design and 1D photonic crystal integration

Baidong Wu, Liyang Yue, Zengbo Wang [*]

School of Computer Science and Engineering, Bangor University, Dean Street, Bangor, Gwynedd LL57 1UT, UK

A B S T R A C T

We present a wide-angle, incident-insensitive metamaterial bandpass filter integrating gold-coated silicon nanospheres (SiNS) with a 1D photonic crystal (1D-PC) edge filter. This hybrid design leverages localized surface plasmon resonance (LSPR) and photonic bandgap engineering to achieve high optical density (OD $\approx$ 2.31) in stopbands while maintaining strong passband transmission (peak T$\approx$ 80%). Unlike conventional thin-film filters, it minimizes blue-shift effects and ensures angle-stable performance up to 60° incidence. These results demonstrate a promising approach for high-performance optical filters in imaging, sensing, and laser protection applications.

1. Introduction

Conventional thin-film optical filters are widely used in various applications due to their high customizability, stability, and low optical loss [1]. However, their performance suffers from significant angular sensitivity, especially the so-called 'blue-shift' effect at high angles of incidence (AOI), where the central transmission wavelength shifts due to changes in admittance and optical path length. This is because thin-film filters operate based on angle-sensitive constructive and destructive interference between alternating dielectric layers [2]. Several approaches have attempted to mitigate this issue by incorporating metal absorptive layers or organic materials [3–7], but these methods often compromise transmission efficiency, angular robustness, or long-term stability.

To address these limitations, metamaterial-based optical filters have emerged as a promising alternative. By engineering artificial subwavelength structures, metamaterials enable tailored dispersion properties, negative refractive indices, and enhanced control over photonic bandgaps [8–11]. These advantages have facilitated their application in terahertz and infrared filtering, GHz permittivity sensing, and advanced photonic crystal engineering. In particular, hyperbolic metamaterials (HMMs)—formed by alternating metal and dielectric layers—can support dispersionless modes that allow angularly insensitive transmission and reflection, especially under TM polarization [12]. These structures are often compatible with existing thin-film deposition techniques and offer a route to wide-angle operation. However, despite these merits, HMMs exhibit notable drawbacks. Firstly, their wide-angle insensitivity applies predominantly to TM-polarized light, limiting their use in unpolarized or TE-dominated systems. Secondly, due to the inherent loss in metal or doped-semiconductor layers used in HMM structures, the overall transmission of bandpass filters reported in the literature remains relatively low (typically 10–40 % for AOI >20°) [13-15]. While some recent studies demonstrate multiple resonance peaks with angular stability in quasi-periodic HMM-based photonic crystals, these designs are not optimized for high-transmission performance and still suffer from reduced transmission at oblique incidence [16]. This highlights the need for alternative metamaterial strategies that can achieve wide-angle operation while maintaining both high transmission efficiency and polarization independence.

In 2018, our group introduced the first 3D metamaterial notch filter based on silver nanoparticles (AgNPs), exploiting localized surface plasmon resonance (LSPR) to achieve strong 532 nm laser blocking (OD > 1.88) and AOI stability up to 85° [17]. This marked a turning point for nanoparticle-based optical filtering. In 2019, Lotti et al. proposed a bandpass design using silicon nanospheres (SiNS) and gold (Au) to form Si-Au core–shell structures, which demonstrated moderate AOI-insensitive behavior [18]. However, their single-meta-layer configuration lacked proper anti-reflection coatings and suffered from performance limitations, including insufficient optical density (OD) above 1050 nm and passband distortion under TE polarization at high AOI.

To overcome these drawbacks, we recently developed a multi-layered nanoparticle-based edge filter incorporating anti-reflection coatings, achieving substantially improved edge suppression and passband clarity [19]. Building on this framework, the current work extends the design to the bandpass filter, with a focus on visible and

* Corresponding author.
E-mail address: z.wang@bangor.ac.uk (Z. Wang).

https://doi.org/10.1016/j.optcom.2025.132185
Received 25 February 2025; Received in revised form 12 June 2025; Accepted 30 June 2025
Available online 1 July 2025
0030-4018/© 2025 The Author(s). Published by Elsevier B.V. This is an open access article under the CC BY license (http://creativecommons.org/licenses/by/4.0/).

near-infrared (NIR) operation. While Lotti's original single-layer bandpass filter demonstrated AOI stability, it exhibited residual transmission above 1050 nm and attenuation around 680 nm under oblique TE incidence.

Here, we propose an integrated hybrid bandpass design consisting of multiple stacked meta-layers (MLs) embedded with gold-coated SiNS, combined with a top 1D photonic crystal (1D-PC) edge filter. The 1D-PC structure is composed of alternating high- and low-refractive-index dielectric layers arranged in a periodic fashion along a single axis. This periodic configuration induces a photonic bandgap (PBG) that prohibits the propagation of specific frequency ranges of light, acting as a spectral barrier. By tuning the layer thickness and refractive index contrast, as well as introducing structural asymmetry or defects, these bandgaps can be precisely controlled, enabling narrowband, angle-stable filtering responses [20]. Such structures have found wide use in modulation, optical sensing and filtering applications due to their high spectral selectivity, compactness, and compatibility with planar fabrication [21-24].

In our design, the 1D-PC functions as an angularly robust edge filter that complements the LSPR-driven spectral shaping provided by the meta-layers. Its inclusion allows further suppression of side lobes near the passband edge (especially in the 600–700 nm range), and its interference-independent operation ensures that performance remains consistent across varying angles of incidence. Although 1D-PC-only wide-angle filters have been previously explored [25-27], their intrinsic limitations in transmission efficiency and limited tuning flexibility make them insufficient alone. By integrating the 1D-PC with plasmonic metastructures, our hybrid approach overcomes these weaknesses and realizes a design with high optical density (ODOD $\approx$ 2.31), strong passband transmission (peak T $>$ 80 %), and angular stability up to 60° under both TE and TM polarization.

While wide-angle photonic filters have been previously demonstrated using either HMMs or 1D-PCs, the combined use of LSPR-active nanoparticle layers with tailored photonic crystal filtering presents a new paradigm. This hybridization provides enhanced control over spectral features, stronger suppression of undesired transmission, and greater polarization insensitivity. Our results demonstrate the feasibility and practical advantages of this strategy for next-generation optical filters suitable for imaging, sensing, and laser protection.

2. Method and models

2.1. Design protocol and methodology

We adopt the same design protocol as in our recently published work, combining full-wave simulations (CST, version 2022) with transfer matrix-based thin-film design (Essential Macleod, ESM, version 10.2) for filter optimization [19]. The challenge lies in accurately approximating the effective complex effective refractive index (n_{eff}) of meta-layers (MLs), as ESM models only homogeneous layers while MLs exhibit spatially varying refractive indices. To address this, we use the Kramers–Kronig (K–K) approximation to extract the real part of complex effective refractive index n'_{eff} from transmission (T) and reflection (R) spectra obtained via CST [28]. The detailed formulation and validation can be found in our previous literature [19].

We follow a four-step methodology, integrating CST simulations with ESM-driven multi-layer refinement.

1 Single-Meta-Layer Optical Response in CST

A unit cell consisting of a SiNS with a gold shell (radius: R_{SiNS}, shell thickness: T_{Shell}) embedded in a silicon nitride (SiN) host medium on a 1200 nm thick glass substrate was built in CST. The boundary condition was set to 'unit cell', forming an infinite primitive cubic lattice. The incident wavelength (λ) ranged from 350 to 1200 nm, with a mesh setting of $\lambda/10$ for the host material and $(R_{SiNS} + T_{Shell})/5$ for the nanoparticles. The incident and output ports were positioned ±3600 nm from the zero plane to emulate real-world conditions. In this work, the SiNS radius R_{SiNS} is fixed at 70 nm, while the gold shell thickness T_{Shell} varies from 15 nm to 20 nm. The refractive indices of all materials used are provided in Supplementary Figure S1, with source data referenced in [29–35].

2 Extraction of Effective Refractive Index (n'_{eff} and k'_{eff}) of Meta-Layers

To integrate MLs into ESM, we extract their effective refractive index using the K-K approximation. The imaginary part (k'_{eff}) is determined from simulated transmission (T) and reflection (R) data, while the real part is computed via the Hilbert transform, as detailed in Refs. [28,36].

$$\frac{1-R}{T} = exp\left(4\pi k'_{eff} d \middle/ \lambda\right) \tag{1}$$

where d and λ denote the thickness of ML and incidence wavelength, respectively.

By using K-K approximation, the unknown real part of a complex refractive index at any frequency (ω') can be determined as long as the imaginary part is known across the entire frequency range (ω).

$$n(\omega) = n_{host} + \frac{2}{\pi} P \int_0^{\infty} \frac{\omega k(\omega) - \omega' k(\omega')}{\omega^2 - \omega'^2} \tag{2}$$

Here, n_{host} is the refractive index of the host medium. The integral in Equation (2)is evaluated using the Hilbert transform method, where P indicates the Cauchy principal value, ensuring the integral remains well-defined by symmetrically excluding the singularity at $\omega=\omega'$.

A comparison of CST-simulated transmission spectra and the K–K model (as shown in Fig. S2) shows strong agreement, with an average MSE of 0.0042, confirming the method's accuracy.

3 Optimization of 1D Photonic Crystal-Based Edge Filter in ESM

With the extracted n_{eff}, two MLs were modelled in ESM, followed by the addition of a photonic crystal-based edge filter. The refinement target was set to zero reflection in the passband (750–850 nm) at 0°, 30°, and 60° AOI (TE polarization) to ensure angle insensitivity. Since blocking performance depends on the SiNS and gold shell, no additional stop-band constraints were imposed.

For efficiency, SimPlex refinement was used, manually removing excessively thick layers (>2 × quarter-wavelength optical thickness) and thin layers (<10 nm) while keeping other parameters at default settings.

4 Cross-Verification and Fine-Tuning in CST

The optimized model was validated in CST, with refinements applied to achieve optimal performance. While CST allows precise thickness adjustments, optimizing multiple parameters is computationally expensive. By leveraging ESM for rapid multi-layer optimization, followed by CST validation, this hybrid approach enables the efficient design of high-performance optical filters combining MLs and thin-film structures.

2.2. Designs

We present a series of metamaterial-based bandpass filter designs, building upon previous single-meta-layer designs to achieve improved blocking performance and angle insensitivity. The unit cell structures are schematically illustrated in Fig. 1, with their corresponding layer configurations detailed in Table 1.

The designs include.

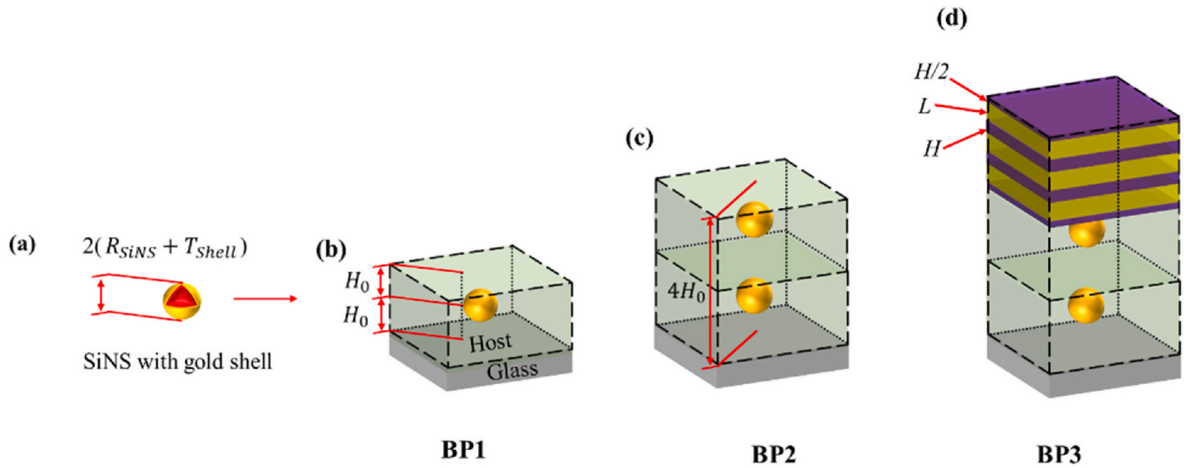

Fig. 1. The schematic illustration of **(b)** singl-ML, **(c)** two-MLs and **(d)** hybrid design with the fundamental gold coated SiNS as shown in **(a)**. (For interpretation of the references to colour in this figure legend, the reader is referred to the Web version of this article.)

Table 1
Bandpass filter designs.

Design ID	Configurations H: High-index layer (quarter-wavelength) L: Low-index layer (quarter-wavelength) M: Meta-layer
BP0	$Air\|1.20(0.5L\,H\,0.5L)^6\;\;1.05(0.5L\,H\,0.5L)^6\;\;0.80(0.5H\,L\,0.5H)^4$ $0.60(0.5H\,L\,0.5H)^4\;0.50(0.5H\,L\,0.5H)^4\;0.40(0.5H\,L\,0.5H)^4\|Glass$ (Fig. S4 (b) and H: TiO_2, L: SiO_2, $\lambda_{Ref} = 750$ nm.)
BP1	$Air\|M\|Glass$ (Fig. 1b)
BP2	$Air\|(M)^2\|Glass$ (Fig. 1c)
BP3	$Air\|(0.5H\,L\,0.5H)^3\|(M)^2\|Glass$ (Fig. 1d–H: α-Si, L: SiN, $\lambda_{Ref} = 600$ nm.)

(a) Fundamental Unit Cell: A silicon nanosphere (SiNS) coated with a gold shell, with a total diameter of $2(R_{SiNS} + T_{Shell})$.
(b) BP1 – Single-Meta-Layer Bandpass Filter (Lotti's Design): A single-ML configuration embedding gold-coated SiNS in a host medium, serving as the baseline reference.
(c) BP2 – Multi-Meta-Layer Bandpass Filter: A two-MLs structure, introduced to enhance blocking performance while maintaining AOI insensitivity, addressing the limitations of BP1.
(d) BP3 – Optimized Bandpass Filter with 1D Photonic Crystal Edge Filter: A further optimized design, incorporating a 1D photonic crystal-based edge filter, significantly improving passband transmission at TE polarization while maintaining strong blocking performance.

3. Results

3.1. Traditional bandpass filter

We begin by demonstrating the classical *blue-shift* phenomenon commonly observed in traditional thin-film bandpass filters currently available on the market. The example presented here, designated as BP0 in Table 1, comprises 76 alternating layers of high-index titanium dioxide (TiO_2) and low-index silicon dioxide (SiO_2), without the use of nanospheres. Both the number of layers and their thicknesses are carefully optimized to achieve high bandpass performance. Any reduction in layer count or deviation from the optimized configuration leads to a notable decline in filtering efficiency, as illustrated in Fig. S5. The complete design process is provided in Fig. S4(b).

Simulation results reveal a significant degradation in performance at oblique angles of incidence. As illustrated in Fig. 2, the filter exhibits a pronounced blue shift of the central wavelength, narrowing of the passband under TE polarization, and diminished stopband blocking under TM polarization. This angular sensitivity is primarily attributed to phase delay variations and the Brewster angle effect. As the incidence angle increases, the effective optical path length within the multilayer stack becomes longer, necessitating a shorter wavelength to satisfy the constructive interference condition. The shifted wavelength can be approximated by the following expression [37]:

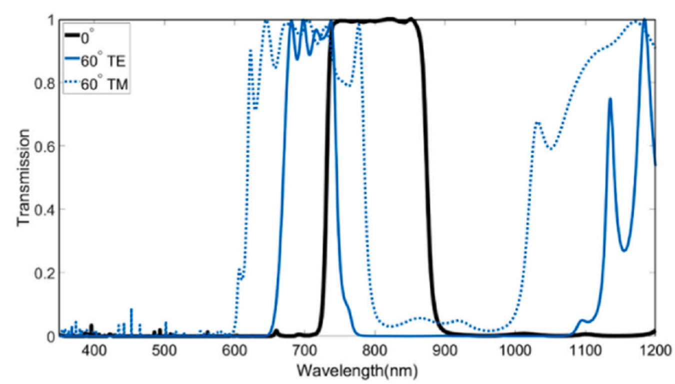

Fig. 2. Transmission spectra of a conventional thin-film bandpass filter under normal incidence (0°) and oblique incidence (60°) for TE and TM polarizations, illustrating the blue-shift and spectral distortion at high angles. (For interpretation of the references to colour in this figure legend, the reader is referred to the Web version of this article.)

$$\lambda_\theta \approx \frac{\lambda_0}{2}\left(\frac{n_{H,\theta}}{n_H} + \frac{n_{L,\theta}}{n_L}\right) \tag{3}$$

where n_H and n_L denote the refractive indices of high- and low-indices material, respectively. $n_{H,\theta}$ and $n_{L,\theta}$ represent the effective indices of materials at AOI of θ. They can be expressed as $n_{H,\theta} = n_H \cos\theta$ and $n_{L,\theta} = n_L \cos\theta$ for TE polarization, and $n_{H,\theta} = n_H \sec\theta$ and $n_{L,\theta} = n_L \sec\theta$ for TM polarization.

3.2. Metamaterial bandpass filters

We now turn to the performance of metamaterial-based filter designs. To aid the understanding of the underlying nanoparticle behavior, we first examined the extinction and transmission characteristics of a single silicon nanosphere ($R_{SiNS} = 70$ nm), with and without a gold shell ($T_{shell} = 20$ nm), embedded in various dielectric environments. These results, summarized in Fig. S3, reveal that bare SiNS exhibits strong electric and magnetic dipole resonances in the short-wavelength region, while the addition of a gold shell introduces a dominant plasmonic response in the NIR. Furthermore, the host refractive index significantly influences both resonance strength and spectral position. This analysis supports the selection of SiNS core and motivates the parameter space used in our design optimization. Although such single-particle models cannot fully capture the complex interactions in periodic arrays, they offer essential physical insights for guiding multilayer configuration choices. These single-particle observations inform the design of periodic structures with enhanced spectral control.

Our metamaterial-based bandpass filter designs (BP1, BP2, BP3) exhibit significantly improved angular performance over conventional filter design (BP0). Fig. 3 presents the contour plots of transmission (T) as a function of wavelength (x-axis) and angle of incidence (y-axis) for TE polarization (left column: a, c, e) and TM polarization (right column: b, d, f). The edge wavelength (λ_{Edge}) is defined as the wavelength where transmission (T) equals $0.5T_{Peak}$, establishing two boundary wavelengths for the passband: $\lambda_{Left\text{-}Edge}$ and $\lambda_{Right\text{-}Edge}$. The central wavelength (λ_c) is then determined as: $\lambda_c = (\lambda_{Left\text{-}Edge} + \lambda_{Right\text{-}Edge})/2$. In this work, the passband extends from 750 to 850 nm, ensuring high transmission, while the stopbands (350–680 nm and 850–1200 nm) maintain low transmission (OD $\geq$ 1, where OD = -log T).

The BP1 design (Fig. 3a and b) replicates Lotti's work in Ref. [18] with a single-ML structure, where H_0 = 150 nm, R_{SiNS} = 70 nm, and T_{Shell} = 20 nm. This design exhibits reasonable angle insensitivity in its passband, with a relatively stable central wavelength under varying AOI. However, it suffers from several performance limitations, particularly in the stopband. Notably, the design demonstrates poor blocking performance in the stopbands, especially for the longer wavelength region ($\geq$1050 nm), where transmission remains high (T > 0.25), as highlighted by regions A and B in Fig. 3a and b, respectively. Additionally, an undesired transmission attenuation band appears between 15° and 60° AOI, as indicated by the green dashed line and zone C in Fig. 3a. Due to the limited tunability of single-ML structures, resolving these issues through parameter adjustments alone is challenging. To overcome these limitations, the introduction of multi-MLs designs and hybrid filtering strategies is crucial, as they provide greater flexibility in tuning optical properties and effectively mitigate performance degradation.

The BP2 design (Fig. 3c and d) was developed to enhance stopband

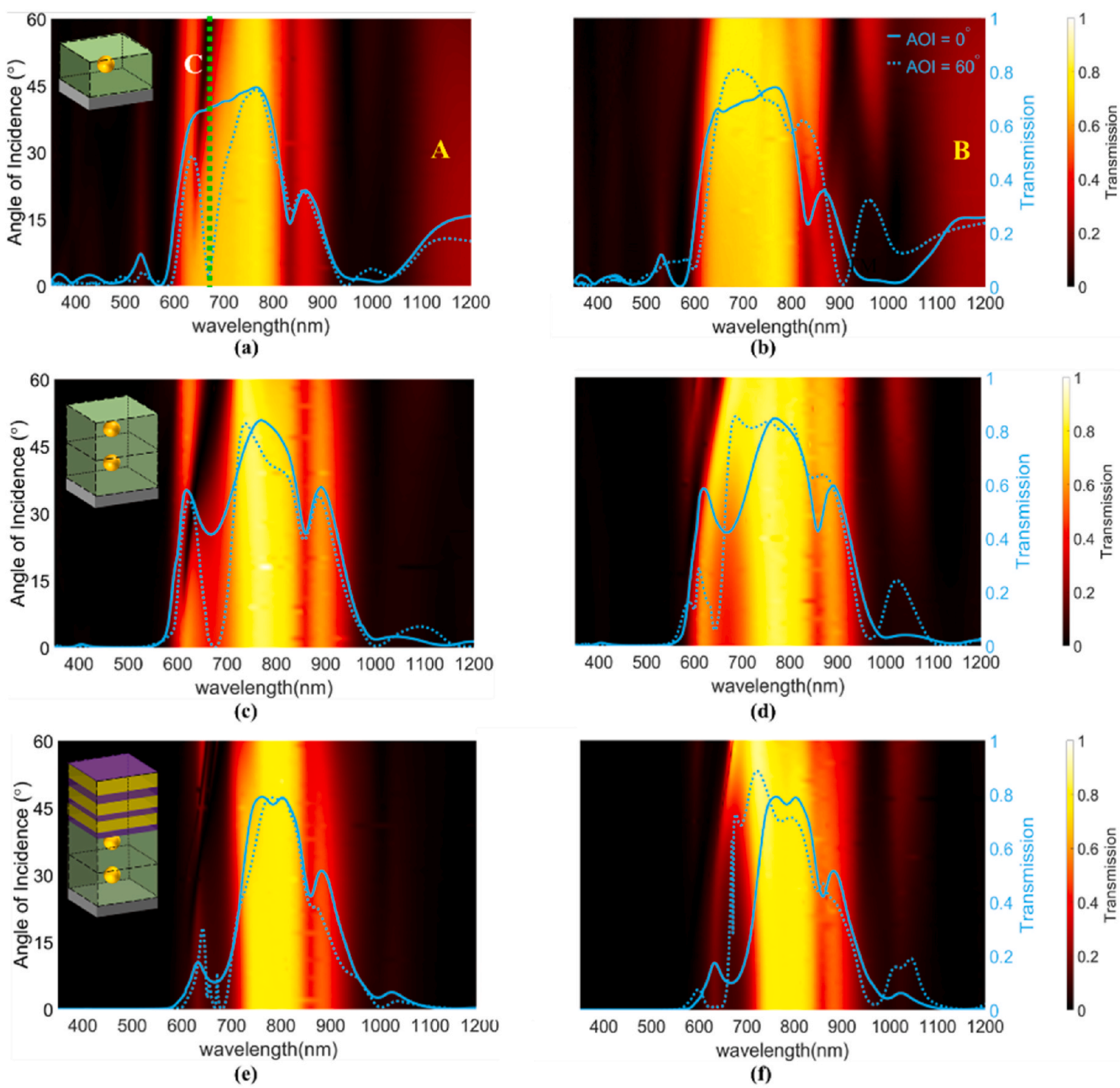

Fig. 3. Contour plots of transmission spectra for BP1 (a, b), BP2 (c, d), and optimized BP3 (e, f) designs under TE (left column) and TM (right column) polarizations. Solid and dashed lines represent transmission at 0° and 60° incidence angles, respectively. Zones A, B, and C in (a, b) indicate critical regions targeted for further optimization.

blocking performance in zones A, B and C by employing a two-MLs structure while keeping all parameters fixed except for a thinner gold shell ($T_{Shell'} = 15$ nm), reduced from the original 20 nm. The optimal shell thickness was determined through CST parametric sweeping, evaluating the transmission response of the two-MLs design under varying gold shell thicknesses at 0° AOI to ensure adequate passband transmission while maintaining reasonable stopband blocking performance. However, this modification resulted in an expansion of the passband width, which is undesirable and is addressed in BP3 design.

BP3 Design: To address the passband broadening in BP2, a 1D ternary photonic crystal-based edge filter $(0.5H\ L\ 0.5H)^3$, where H and L represent quarter-wavelength thickness layers of high-index (α-Si) and low-index (TiO_2) materials with a reference wavelength of 600 nm, was deposited on top of BP2. The objective was to suppress the peaks (Zone C) on the left edge of the passband, leading to a narrowed passband with sharper spectral edges, as seen in both Fig. 3e, f and Fig. S6.

The integration of the edge filter with the BP2 design required optimization of the layer thickness to maximize overall device performance. This was achieved using ESM software's needle synthesis optimization function for multi-layered structures. The detailed thicknesses for unoptimized and optimized designs are provided in Table S1.

The optimized filter exhibits significant suppression of Zone C within the 600–700 nm range under TE-polarized incidence (Fig. 3e), ensuring a well-defined passband with minimal spectral distortion. Under TM-polarized incidence (Fig. 3f), the passband slightly shifts toward shorter wavelengths due to the Brewster angle effect. However, the overall performance remains substantially improved compared to BP2, demonstrating the effectiveness of this hybrid approach. The combination of a classical photonic crystal edge filter with a core-shell nanoparticle-based metamaterial thus presents an effective strategy for addressing optical filtering challenges.

3.3. Comparison of filter performances

We now compare the performance of the three filters (BP1, BP2, BP3) in terms of stopband optical density (OD) and passband transmission (T) as a function of AOI, as shown in Fig. 4.

Stopband: The blocking performance improves significantly as additional meta-layers and the edge filter are introduced. The average OD increases from approximately 1.50 to over 2.00, and finally 2.25+ for all AOI, demonstrating the effectiveness of these modifications. For TM polarization, the average OD improvement achieved by the two-MLs design and the BP3 design with an additional edge filter is 0.60 ± 0.10 and 0.80 ± 0.10, respectively. These results confirm that increasing the number of MLs enhances blocking performance, while integrating an edge filter further improves OD in the shorter wavelength region. This effect is particularly pronounced for TE-polarized light at high AOI, as evidenced by a more substantial OD increase in these conditions.

Passband: For TM-polarized incidence, the transmission performance of all three designs remains stable, with no significant variation observed. However, the final BP3 design exhibits a more pronounced improvement in TE-polarized transmission at high AOI, as the edge filter leads to a more continuous passband under these conditions. The introduction of a second ML alone does not enhance transmission, as the optical admittance is not optimized to match that of air. This highlights the crucial role of further optimization using ESM, which ensures a well-matched optical interface and significantly improves transmission characteristics.

Next, we compare the central wavelength shift of the passband as a function of the incident angle, as presented in Fig. 5. Firstly, all metamaterial-based designs (BP1–BP3) exhibit significantly improved angular stability compared to the classical thin-film design (BP0), where a flat line indicates minimal wavelength shift.

For TE polarization, the final optimized BP3 design demonstrates near shift-free performance, as evident from the flat horizontal line in Fig. 5a. However, for TM polarization (Fig. 5b), the angular stability of BP3 degrades, becoming comparable to BP1, indicating a weaker performance improvement under TM incidence.

Finally, the tunability of the designed filter is illustrated in Fig. S7. While the full simulation results are presented in the figure, the observed trends are relatively complex. Here, we highlight the most representative effects for clarity. As shown in S7(a), increasing the radius of SiNSs

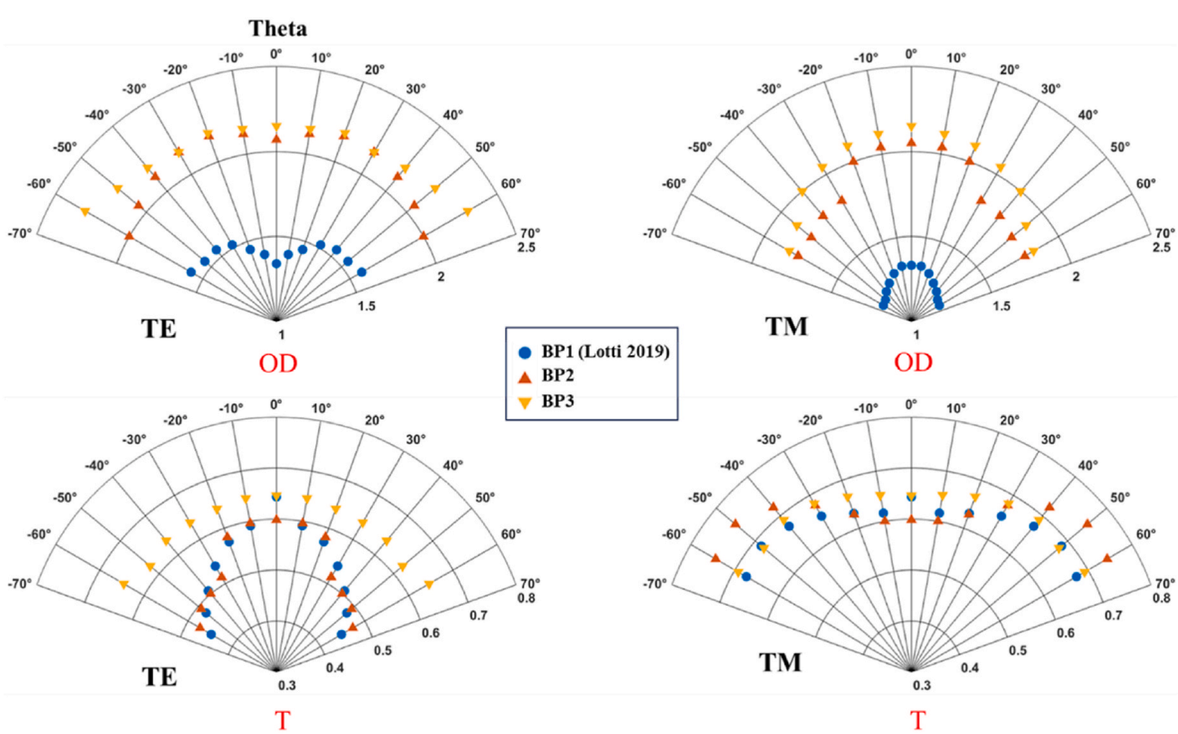

Fig. 4. (a, b) Average optical density (OD) for the stopband and (c, d) average transmission for the passband of three bandpass filters (BP1, BP2, BP3) under varying angles of incidence (AOI, represented as Theta) for both TE (left) and TM (right) polarized light. The BP1 design (Lotti et al., 2019) is reproduced from Ref. [18].

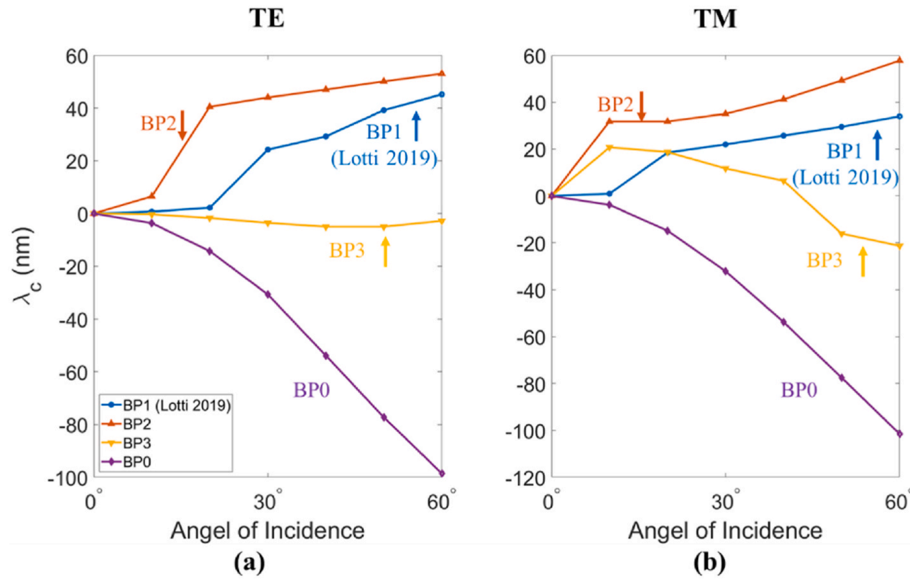

Fig. 5. Comparison of passband central wavelength shift for BP0, BP1, BP2, and BP3 under TE (a) and TM (b) polarization as a function of AOI.

with a fixed gold shell thickness (T_{shell}= 15 nm) leads to a red-shift and broadening of the passband, accompanied by enhanced transmission. In contrast, S7(b) shows that when the SiNS radius (R_{SiNS}= 70 nm) is held constantly, reducing the gold shell thickness weakens the plasmonic resonance, resulting in diminished blocking in the longer wavelength region. As the shell thickness increases, the original passband narrows and eventually vanishes, while a new passband emerges in the near-infrared (NIR) range.

3.4. Discussions

Despite the significant improvements achieved through our multi-meta-layer and hybrid design, the performance under TM-polarized light at oblique incidence remains less robust than for TE polarization. This limitation arises primarily from the intrinsic polarization sensitivity of the core–shell resonance mechanisms. In this context, HMMs have shown considerable promise for achieving angular insensitivity under TM polarization, owing to their support of dispersionless modes enabled by anisotropic permittivity profiles [14,16]. Nevertheless, the practical implementation of HMMs is hindered by their inherently low transmission efficiency and strong polarization dependence. A potential future direction lies in the integration of HMM-inspired multilayer structures with nanoparticle-based meta-layers, forming a hybrid platform that could potentially extend polarization tolerance while maintaining high transmission—an area that remains largely unexplored.

Another promising route involves the exploration of alternative materials and further structural refinement. The silicon–gold core–shell configuration adopted in this work provides a balance of high-index dielectric resonance and plasmonic response, enabling broadband spectral tunability. Silicon offers a high refractive index with minimal loss in the near-infrared (NIR), while gold provides a stable and well-characterized plasmonic behavior. While effective, this combination is not exclusive. Alternative core materials such as gallium phosphide (GaP), germanium (Ge), or TiO_2, and alternative shell materials including silver (Ag) or aluminum (Al), may offer improved performance in different spectral regimes or for specific application requirements. Similarly, although SiN was selected as the host medium for its moderate refractive index and fabrication compatibility, other dielectrics such as SiO_2 or aluminum oxide (Al_2O_3) may also be viable depending on target wavelength ranges and integration needs. These options underscore the versatility of our design framework and open opportunities for further optimization.

From a fabrication perspective, block copolymers (BCPs), such as polystyrene-b-poly(ethylene oxide) (PS-b-PEO), have demonstrated strong potential for forming highly ordered porous nanostructures via annealing-driven self-assembly [38,39]. Compared to conventional lithographic techniques, BCP self-assembly is significantly more cost-effective and scalable. Our group has successfully employed this method to fabricate large-area metafilms for AgNP-based notch filters with interstitial spacings as small as 30 nm [40]. Recent advances have also extended BCP methods to multilayer assembly—up to three layers—providing practical feasibility for scalable ML production [41]. To address fabrication-related uncertainties, particularly those associated with reproducibility, interlayer alignment, and structural uniformity, we are currently investigating in situ monitoring strategies and statistical process control techniques. These efforts aim to enhance process reliability, ensure consistency across substrates, and facilitate high-yield production of complex metamaterial structures.

4. Conclusion

In conclusion, we successfully optimized a wide-angle bandpass filter, addressing challenges in blocking efficiency and transmission stability at varying AOI. The optimization process, incorporating a multi-MLs design, a photonic crystal-based edge filter, and a hybrid design protocol, significantly enhances performance. The final design achieves higher blocking efficiency, with optical densities of 2.31 (AOI = 60°, TE) and 1.83 (AOI = 60°, TM), while maintaining near shift-free angular performance and improved average transmission (44 %–65 % and peak transimssion (80%) under TE polarization. These enhanced optical properties make the filter well-suited for applications requiring consistent performance across a wide range of AOI. This work contributes to the advancement of high-efficiency metamaterial optical components, offering greater performance, stability, and adaptability for diverse optical filtering applications.

CRediT authorship contribution statement

Baidong Wu: Writing – original draft, Software, Methodology, Investigation, Formal analysis, Conceptualization. **Liyang Yue:** Writing – review & editing, Validation, Project administration. **Zengbo Wang:** Writing – review & editing, Validation, Supervision, Software, Project administration, Methodology, Funding acquisition, Conceptualization.

Declaration of competing interest

The authors declare that they have no known competing financial interests or personal relationships that could have appeared to influence the work reported in this paper.

Acknowledgements

Leverhulme Trust (RF-2022-659); Royal Society (IEC\R2\202178); Bangor University (BUIIA-S46910).

Appendix A. Supplementary data

Supplementary data to this article can be found online at https://doi.org/10.1016/j.optcom.2025.132185.

Data availability

Data will be made available on request.

References

[1] T.C. Brelje, et al., in: B. Matsumoto (Ed.), Multicolor Laser Scanning Confocal Immunofluorescence Microscopy: Practical Application and Limitations, secondMethods in Cell Biology, 70, Academic Press., California, United States, 2002, pp. 165–244.

[2] H. Macleod, Thin-Film Optical Filters, fourth ed., CRC Press, Boca Raton, United States, 2010, pp. 299–401.

[3] J. Liu, et al., Design and numerical simulation of a bandpass filter nano-film, Chinese, J. Phys. 69 (2021) 430–439.

[4] C. Ji, et al., Engineering light at the nanoscale: structural color filters and broadband perfect absorbers, Adv. Opt. Mater. 5 (20) (2017) 1700368.

[5] K.T. Lee, et al., Wide-angle, polarization-independent ultrathin broadband visible absorbers, Appl. Phys. Lett. 108 (3) (2016) 031107.

[6] Y.J. Jen, M.j. Lin, Design and fabrication of a narrow bandpass filter with low dependence on angle of incidence, coatings 8 (7) (2018) 231.

[7] K. Liu, et al., Super absorption of ultra-thin organic photovoltaic films, Opt. Commun. 314 (2014) 48–56.

[8] A.H. Aly, et al., Cutoff frequency in metamaterials photonic crystals within Terahertz frequencies, Int. J. Mod. Phys. E 31 (15) (2017) 1750123.

[9] A.H. Aly, et al., Photonic crystal enhanced by metamaterial for measuring electric permittivity in GHz range, photonics 8 (10) (2021) 416.

[10] A.G. Mohamed, et al., Multiplication of photonic band gaps in one-dimensional photonic crystals by using hyperbolic metamaterial in IR range, Sci. Rep. 13 (2023) 324.

[11] A.H. Aly, et al., Analysis of cutoff frequency in a one-dimensional superconductor-metamaterial photonic crystal, Physica C: Superconductivity and its Applications 528 (2016) 5–8.

[12] C.H. Xue, et al., Dispersionless gaps and cavity modes in photonic crystals containing hyperbolic metamaterials, Phys. Rev. B 93 (2016) 125310.

[13] F. Wu, et al., Experimental demonstration of angle-independent gaps in one-dimensional photonic crystals containing layered hyperbolic metamaterials and dielectrics at visible wavelengths, Appl. Phys. Lett. 112 (2018) 041902.

[14] M.A. Abdulkareem, et al., Integrated optical filters with hyperbolic metamaterials, Nanomaterials 13 (4) (2023) 759.

[15] B. Wells, et al., Angle-insensitive plasmonic nanorod metamaterial-based band-pass optical filters, Opt. Express 29 (2021) 11562–11569.

[16] A.G. Mohamed, et al., A combination of angle insensitive stopband/passband filters based on one-dimensional hyperbolic metamaterial quasiperiodic photonic crystals, RSC Adv. 13 (27) (2023) 18238–18252.

[17] J.N. Monks, et al., A wide-angle shift-free metamaterial filter design for anti-laser striking application, Opt. Commun. 429 (2018) 53–59.

[18] F. Lotti, et al., Nanoparticle-based metasurfaces for angular-independent spectral filtering applications, J. Appl. Phys. 126 (21) (2019) 213101.

[19] B. Wu, et al., Optimized wide-angle metamaterial edge filters: enhanced performance with multi-layer designs and anti-reflection coatings, Photonics 11 (5) (2024) 446.

[20] K.T. Lee, et al., Angular- and polarization-independent structural colors based on 1D photonic crystals, Laser & Photonics, Rev 9 (3) (2015) 354–362.

[21] M.M. Abadla, et al., Thermo-optical properties of binary one dimensional annular photonic crystal including temperature dependent constituents, Physica E: Low-Dimens. Syst. Nanostruct. 119 (2020) 114020.

[22] A.H. Aly, et al., Defect mode tunability based on the electro-optical characteristics of the one-dimensional graphene photonic crystals, Appl. Opt. 59 (16) (2020) 4796–4805.

[23] M.M. Abadla, et al., Detection and sensing of hemoglobin using one-dimensional binary photonic crystals comprising a defect layer, Appl. Opt. 59 (2) (2020) 418–424.

[24] O.A. Abd El-Aziz, et al., One-dimensional defective photonic crystals for the sensing and detection of protein, Appl. Opt. 58 (30) (2019) 8309–8315.

[25] X. F Xu, J.Y. Ding, A wide band-pass filter of broad angle incidence based on one-dimensional metallo-dielectric ternary photonic crystal, Opt. Quant. Electron. 41 (2009) 1027–1032.

[26] C.H. Chen, et al., Wide-field-of-view GaAsAlxOy one-dimensional photonic crystal filter, Appl. Opt. 44 (8) (2005) 1503–1511.

[27] T. Xu, et al., Nearly polarization-insensitive angular filters enabled by metal-dielectric photonic crystal in the visible region, Appl. Opt. 63 (15) (2024) 4044–4048.

[28] J.E. Bertie, S.L. Zhang, Infrared intensities of liquids. ix. the Kramers–Kronig transform, and its approximation by the finite Hilbert transform via Fast Fourier transforms, Can. J. Chem. 70 (1992) 520–531.

[29] C. Ji, et al., Decorative near-infrared transmission filters featuring high-efficiency and angular-insensitivity employing 1D photonic crystals, Nano Res. 12 (2019) 543–548.

[30] C. Schinke, et al., Uncertainty analysis for the coefficient of band-to-band absorption of crystalline silicon, AIP Adv. 5 (2015) 067168.

[31] M.R. Vogt, et al., Measurement of the optical constants of soda-lime glasses in dependence of iron content, and modeling of iron-related power losses in crystalline Si solar cell modules, IEEE J. Photovoltaics 6 (2016) 111–118.

[32] L.V. Rodríguez-de Marcos, et al., Self-consistent optical constants of SiO_2 and Ta_2O_5 films, Opt. Mater. Express 11 (2016) 3622–3637.

[33] S.V. Zhukovsky, et al., Experimental demonstration of effective medium approximation breakdown in deeply subwavelength all-dielectric multilayers, Phys. Rev. Lett. 115 (2015) 177402.

[34] L.Y. Beliaev, et al., Optical, structural and composition properties of silicon nitride films deposited by reactive radio-frequency sputtering, low pressure and plasma-enhanced chemical vapor deposition, Thin Solid Films 763 (2022) 139568.

[35] M.N. Polyanskiy, Refractiveindex.info database of optical constants, Sci. Data 11 (1) (2024) 94.

[36] W.Q. Hong, Extraction of extinction coefficient of weak absorbing thin films from special absorption, J. Phys. D Appl. Phys. 22 (1989) 384–1385.

[37] R. Benz, et al., Optimizing thin-film material combinations for immersed narrow-bandpass filters in the VIS and NIR range, in: Proc. SPIE 13020, Advances in Optical Thin Films, vol. III, 2024.

[38] A. Selkirk, et al., Optimization and control of large block copolymer self-assembly via precision solvent vapor annealing, Macromolecules 54 (3) (2021) 1203–1215.

[39] M. Stefik, et al., Block copolymer self-assembly for nanophotonics, Chem. Soc. Rev. 44 (15) (2015) 5076–5091.

[40] J.N. Monks, Shift-free wide-angle metamaterial narrowband filters for anti-laser striking applications, Doctor of Philosophy Thesis (2020).

[41] A. Tavakkoli, K. G, et al., Multilayer block copolymer meshes by orthogonal self-assembly, Nat. Commun. 7 (2016) 10518.